THE ASTRONOMICAL JOURNAL, 169:166 (15pp), 2025 March https://doi.org/10.3847/1538-3881/ada26a

TESS Hunt for Young and Maturing Exoplanets (THYME). XII. A Young Mini-Neptune on the Upper Edge of the Radius Valley in the Hyades Cluster

Adam Distler[1], Melinda Soares-Furtado[20,1,2], Andrew Vanderburg[2], Jack Schulte[3], Juliette Becker[1], Andrew W. Mann[4], Steve B. Howell[5], Adam L. Kraus[6], Ronan Kerr[7], Khalid Barkaoui[8,9,10], César Briceño[11], Karen A. Collins[12], Dennis Conti[13], Jon M. Jenkins[5], Mary Anne Limbach[14], Samuel N. Quinn[12], Richard P. Schwarz[12], Sara Seager[2,9,15], Jake D. Turner[16], Joseph D. Twicken[5,17], Joshua N. Winn[18], and Carl Ziegler[19,20]

[1] Department of Astronomy, University of Wisconsin–Madison, 475 N. Charter Street, Madison, WI 53706, USA; ajdistler@wisc.edu
[2] Department of Physics and Kavli Institute for Astrophysics and Space Research, Massachusetts Institute of Technology, Cambridge, MA 02139, USA
[3] Center for Data Intensive and Time Domain Astronomy, Department of Physics and Astronomy, Michigan State University, East Lansing, MI 48824, USA
[4] Department of Physics & Astronomy, The University of North Carolina at Chapel Hill, Chapel Hill, NC 27599-3255, USA
[5] NASA Ames Research Center, Moffett Field, CA 94035, USA
[6] Department of Astronomy, The University of Texas at Austin, Austin, TX 78712, USA
[7] Dunlap Institute for Astronomy & Astrophysics, University of Toronto, Toronto, ON M5S 3H4, Canada
[8] Astrobiology Research Unit, Université de Liège, Allée du 6 Août 19C, B-4000 Liège, Belgium
[9] Department of Earth, Atmospheric and Planetary Sciences, Massachusetts Institute of Technology, Cambridge, MA 02139, USA
[10] Instituto de Astrofísica de Canarias (IAC), Calle Vía Láctea s/n, 38200, La Laguna, Tenerife, Spain
[11] Cerro Tololo Inter-American Observatory, Casilla 603, La Serena, Chile
[12] Center for Astrophysics |Harvard & Smithsonian, 60 Garden Street, Cambridge, MA 02138, USA
[13] American Association of Variable Star Observers (AAVSO), 185 Alewife Brook Parkway, Suite 410, Cambridge, MA 02138, USA
[14] Department of Astronomy, University of Michigan, Ann Arbor, MI 48109, USA
[15] Department of Aeronautics and Astronautics, MIT, 77 Massachusetts Avenue, Cambridge, MA 02139, USA
[16] Department of Astronomy and Carl Sagan Institute, Cornell University, Ithaca, NY, USA
[17] SETI Institute, Mountain View, CA 94043, USA
[18] Department of Astrophysical Sciences, Princeton University, Princeton, NJ 08544, USA
[19] Department of Physics, Engineering and Astronomy, Stephen F. Austin State University, 1936 North Street, Nacogdoches, TX 75962, USA
Received 2024 October 15; revised 2024 December 11; accepted 2024 December 20; published 2025 February 25

Abstract

We present the discovery and characterization of TOI-4364b, a young mini-Neptune in the tidal tails of the Hyades cluster, identified through TESS transit observations and ground-based follow-up photometry. The planet orbits a bright M dwarf ($K = 9.1$ mag) at a distance of 44 pc, with an orbital period of 5.42 days and an equilibrium temperature of 488^{+9}_{-7} K. The host star's well-constrained age of 710 Myr makes TOI-4364b an exceptional target for studying early planetary evolution around low-mass stars. We determined a planetary radius of $2.01^{+0.10}_{-0.08}\ R_{\oplus}$, indicating that this planet is situated near the upper edge of the radius valley. This suggests that the planet retains a modest H/He envelope. As a result, TOI-4364b provides a unique opportunity to explore the transition between rocky super-Earths and gas-rich mini-Neptunes at the early stages of evolution. Its radius, which may still evolve as a result of ongoing atmospheric cooling, contraction, and photoevaporation, further enhances its significance for understanding planetary development. Furthermore, TOI-4364b's moderately high transmission spectroscopy metric of 44.2 positions it as a viable candidate for atmospheric characterization with instruments such as JWST. This target has the potential to offer crucial insights into atmospheric retention and loss in young planetary systems.

Unified Astronomy Thesaurus concepts: Exoplanet evolution (491); Exoplanet astronomy (486); Exoplanet detection methods (489); Transit photometry (1709); Stellar rotation (1629); Exoplanet atmospheres (487)

1. Introduction

Investigations of young exoplanets offer crucial insights into the rapid evolutionary changes that occur within the first few hundred million years after the formation of a planet. During this early period, planets undergo significant transformations in their orbital dynamics (e.g., J. E. Chambers & G. W. Wetherill 1998; F. C. Adams & G. Laughlin 2006; A. Morbidelli et al. 2012), structural properties (E. S. Kite et al. 2009), and atmospheric composition and structure (e.g., J. E. Owen & Y. Wu 2017; C. Dorn et al. 2018; S. Ginzburg et al. 2018).

To investigate these early evolutionary processes, the TESS Hunt for Young and Maturing Exoplanets (THYME; E. R. Newton et al. 2019) collaboration focuses on detecting and characterizing transiting exoplanets within young stellar groups and open clusters. These environments are advantageous because the ages, distances, and metallicities of the stars are well constrained, enabling more accurate exoplanetary and host star parameters. Consequently, the young exoplanets identified by THYME and similar surveys serve as key benchmarks for testing theories of exoplanet formation, migration, and evolution.

The nearby Hyades cluster, located at a distance of 46 pc and estimated to be ≈700 Myr old (W. Brandner et al. 2023), is an ideal target for this search. In this work, we present the

[20] NASA Hubble Postdoctoral Fellow.

Table 1
TESS Photometry Used in the Detection and Characterization of TOI-4364b

TESS Data Overview				
Sector	Cadence	Camera	CCD	Observation Dates
5	120 s	1	2	2018 Nov 11–Dec 6
32	120 s	1	2	2020 Nov 20–Dec 15

discovery, characterization, and follow-up observations of a planet in the tidal tails of the Hyades cluster. This planet, TOI-4364b, is the eighth detected in the cluster, joining K2-25 b (A. W. Mann et al. 2016), K2-136 b/c/d (D. R. Ciardi et al. 2018; A. W. Mann et al. 2018), HD 283869b (A. Vanderburg et al. 2018), HD 285507b (S. N. Quinn et al. 2014), and HD 28305b (B. Sato et al. 2007). Although membership in the Hyades has been questioned for HD 28305 (H. M. Tabernero et al. 2012; S. Rser et al. 2019) and HD 283869 (S. T. Douglas et al. 2014; S. Oh & N. W. Evans 2020; L. Long et al. 2023), we include these stars as Hyades members in the figures presented in this work.

TOI-4364b is found in this work to be a transiting mini-Neptune with a 5.42-day orbit around an M dwarf. With a radius of $2.01^{+0.10}_{-0.08}\ R_{\oplus}$, this planet resides at the upper edge of the radius valley (B. J. Fulton et al. 2017), a region where planets with radii between 1.5 and 2.0 $R_{\oplus}$ are scarce. Typically, planets smaller than the lower bound are rocky, while those larger than the upper bound are gaseous mini-Neptunes. Some of the most widely accepted mechanisms proposed to drive the formation of the radius valley are photoevaporation (J. E. Owen & Y. Wu 2017; R. Burn et al. 2024) and core-powered mass loss (S. Ginzburg et al. 2018).

The youth and K-band brightness ($K = 9.1$ mag) of this newly discovered planetary system make it a compelling target for follow-up observations. As a young mini-Neptune on the upper edge of the radius valley, TOI-4364b provides a unique opportunity to explore atmospheric properties and the processes shaping planetary evolution, with its bright, young M dwarf host offering valuable insights into atmospheric retention and loss during the early stages of planetary formation.

The manuscript is structured as follows: Section 2 details the data products used for the detection and characterization of this system. Section 3 focuses on the characterization of stellar properties of TOI-4364, along with the analysis of TOI-4364b and its orbit. Section 4 examines potential false-positive scenarios. Section 5 discusses TOI-4364b in the context of other Hyades planets and within the broader census of exoplanet discoveries.

2. Data

To investigate potential planetary transits of the Hyades star TOI-4364, we used photometric data from the Transiting Exoplanet Survey Satellite (TESS; G. R. Ricker et al. 2015), photometry and radial velocity (RV) measurements from ground-based facilities, and high-resolution speckle imaging.

2.1. The TOI-4364 TESS Light Curve

The TESS survey divides the sky into rectangular sectors. Each sector covers a field of view of 24° × 96° over a baseline of approximately 27 days. To date, TOI-4364 (TIC 4070275) has been observed in Sector 5 and Sector 32 (start dates: 2018 November 11 and 2020 November 20). The data are available with a time sampling of 120 s. Table 1 lists the relevant sectors, cadence, camera number, CCD number, and date range corresponding to these observations.

The data from both sectors were reduced and analyzed by the Science Processing Operations Center (SPOC) at NASA Ames Research Center (J. M. Jenkins et al. 2016). On 2021 May 27, SPOC conducted a transit search of the combined light curve from the two sectors, using an adaptive, noise-compensating matched filter (J. M. Jenkins 2002; J. M. Jenkins et al. 2010, 2020). This resulted in a threshold crossing event with a 5.42-day period. An initial limb-darkened transit model was fitted (J. Li et al. 2019), and a suite of diagnostic tests were performed to help assess the planetary nature of the signal (J. D. Twicken et al. 2018). The transit signature passed all diagnostic tests in the SPOC Data Validation reports, and the source of the transit signal was localized within 1″.23 ± 3″.61 of the target star. The TESS Science Office (TSO) reviewed the vetting information and issued an alert for TOI-4364.01 on 2021 August 5.

For young, active stars, specialized processing can significantly mitigate TESS light-curve noise. We performed additional systematic corrections to the SPOC simple aperture photometry light curve (J. D. Twicken et al. 2010; R. L. Morris et al. 2020) using the method outlined by Vanderburg et al. (2019). This approach involved simultaneously fitting a basis spline with 0.3-day intervals to model the low-frequency stellar variability, along with several vectors describing spacecraft systematics. These vectors included the mean and standard deviation of the quaternion time series to correct for pointing jitter.

We also incorporated cotrending vectors from SPOC's band 3 correction to address fast timescale variations (J. C. Smith et al. 2012; M. C. Stumpe et al. 2012; M. C. Stumpe et al. 2014) and included a 0.1-day high-pass-filtered version of the background flux time series in the decorrelation. We performed a linear least-squares fit to the light curve and removed the contributions of the systematics vectors to produce a cleaned light curve. We then removed the high-frequency stellar variability by subtracting a basis spline fit at 0.5-day breakpoints. The processed data along with a phase-folded light curve are shown in Figure 1.

Flux contamination from neighboring sources can substantially alter the derived planetary parameters. Using `tpfplotter` (A. Aller et al. 2020), which merges Gaia DR3 and TESS data, we generated crowding maps as shown in Figure 2. To account for this dilution, the SAP light curve is corrected using the CROWDSAP metrics from the PDC light curve. These values were 10.76% and 14.02% for Sectors 5 and 32, respectively.

Following these corrections, we searched the light curve for box-shaped dips in brightness using the box-least-squares (BLS) algorithm (G. Kovács et al. 2002), investigating a period range of 0.4–26 days. A compelling 5.42-day signal was apparent at a statistical significance of 11.95, calculated following the method of 2023. To search for additional companions, we masked the transits predicted by the BLS algorithm and did not recover a noticeable signal upon performing the algorithm again.

In addition, we explored the existing transit signals using the Transit Least Squares[21] (TLS) algorithm (M. Hippke &

[21] https://transitleastsquares.readthedocs.io

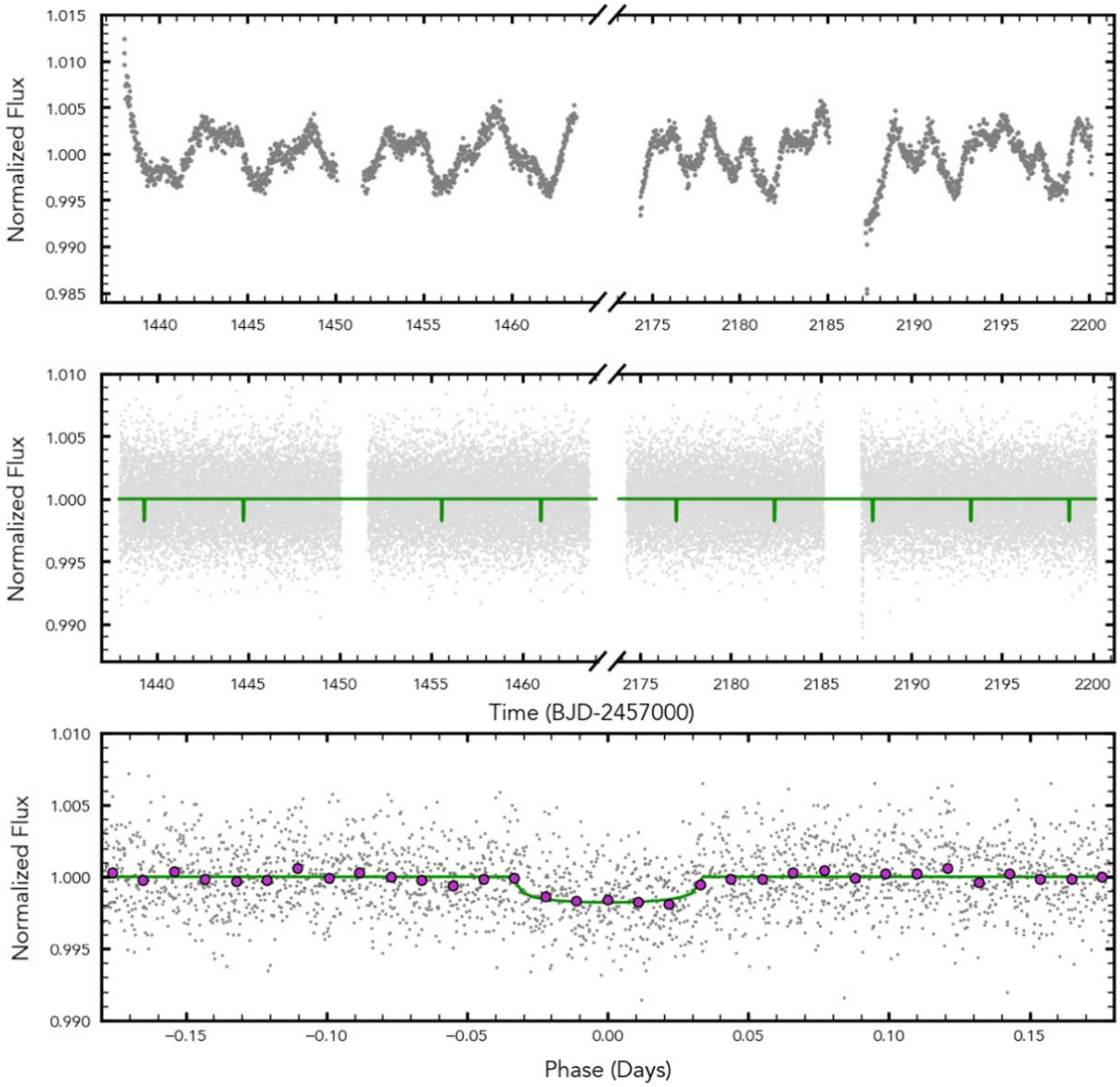

Figure 1. TESS light-curve analysis for TOI-4364b. Top: unflattened, processed light curve of TOI-4364. Middle: flattened, systematically corrected light curve (gray) with the best-fit batman (green). Bottom: phase-folded light curve with binned points (purple) and the phase-folded best-fit transit model (green).

R. Heller 2019). By incorporating considerations such as limb-darkening effects with transit ingress and egress, the TLS algorithm can more accurately model transit shapes, leading to improved detection efficiency. Using the TLS algorithm, we again recovered the transit signal with the same ephemeris. We attribute the observed periodic signal to the detection of a new planet candidate, TOI-4364b, with a transit depth of approximately 2 ppt. This is consistent with the transit depth expected from a mini-Neptune companion.

2.2. Ground-based Seeing-limited Photometry

Follow-up observations using instruments with smaller pixel plate scales can help determine the source of a potential planetary signal. This is important given the large pixel plate scale of TESS. Moreover, planetary transit parameters can be refined by reducing third-light contamination (see D. R. Ciardi et al. 2015), and the ephemeris can be more accurately constrained. Follow-up photometric observations were conducted using several 1.0 m telescopes from the Las Cumbres Observatory Global Telescope (LCOGT; T. M. Brown et al. 2013) Network—a worldwide array of robotic telescopes designed for continuous sky monitoring. Each telescope is equipped with Sinistro cameras, optimized for high-precision photometry. Observations were made at four sites: the South African Astronomical Observatory (SAAO), the Cerro Tololo Inter-American Observatory (CTIO), the Siding Spring Observatory (SSO), and the Teide Observatory. The details of these observations are summarized in Table 2.

Over 6 months, seven observing sessions were carried out, with six capturing the full transit and one focusing on the planet's egress. All observations were performed using the *i'* filter, ensuring consistent data quality across sites. The science data reduction was performed using the standard LCOGT BANZAI pipeline (C. McCully et al. 2018). Photometric measurements were extracted using uncontaminated apertures, ranging between 4$''$.0 and 6$''$.6, using the AstroImageJ[22] software (K. A. Collins et al. 2017). These small apertures were chosen to exclude contamination from a nearby (~11$''$) neighbor that was present in the SPOC apertures. Gaia DR3 identified no

[22] https://www.astro.louisville.edu/software/astroimagej

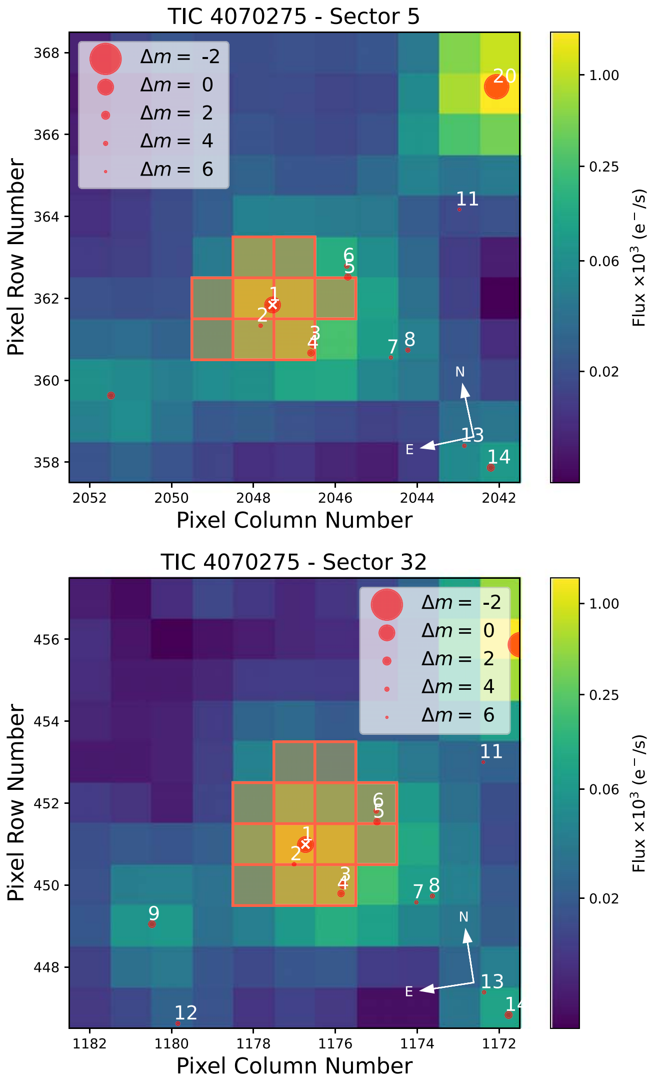

Figure 2. Top panel: crowding map of TOI-4364 for Sector 5, displaying neighboring sources up to a magnitude difference of $\Delta m = 6$. The SPOC aperture is indicated by red squares. Bottom panel: same as the top panel, but for Sector 32.

Table 2
Follow-up Ground-based Photometry of TOI-4364b

Las Cumbres Observatory Global Telescope Network					
Location	Duration	Coverage	Aperture	Date	SNR[a]
SAAO[b]	191 minutes	Full	5.″4	03/15/2022	13.1
CTIO[c]	208 minutes	Full	5.″1	02/22/2022	16.7
SAAO	234 minutes	Full	5.″1	02/05/2022	16.9
SSO[d]	174 minutes	Full	5.″1	12/24/2021	12.6
SAAO	177 minutes	Full	4.″0	10/14/2021	9.2
Teide	189 minutes	Full	5.″0	10/03/2021	15.7
CTIO	165 minutes	Egress	6.″6	09/23/2021	14.4

Notes.
[a] Calculated using the SNR defined in D. Kipping (2023) and the best-fit model from the `EXOFASTv2` output (see Section 3.3).
[b] South African Astronomical Observatory.
[c] Cerro Tololo Inter-American Observatory.
[d] Siding Spring Observatory.

contaminating sources brighter than $G_{\rm Gaia} = 21$ mag closer than this neighbor. The transits were detected convincingly (signal-to-noise ratio (SNR) > 10) in six of the seven follow-up

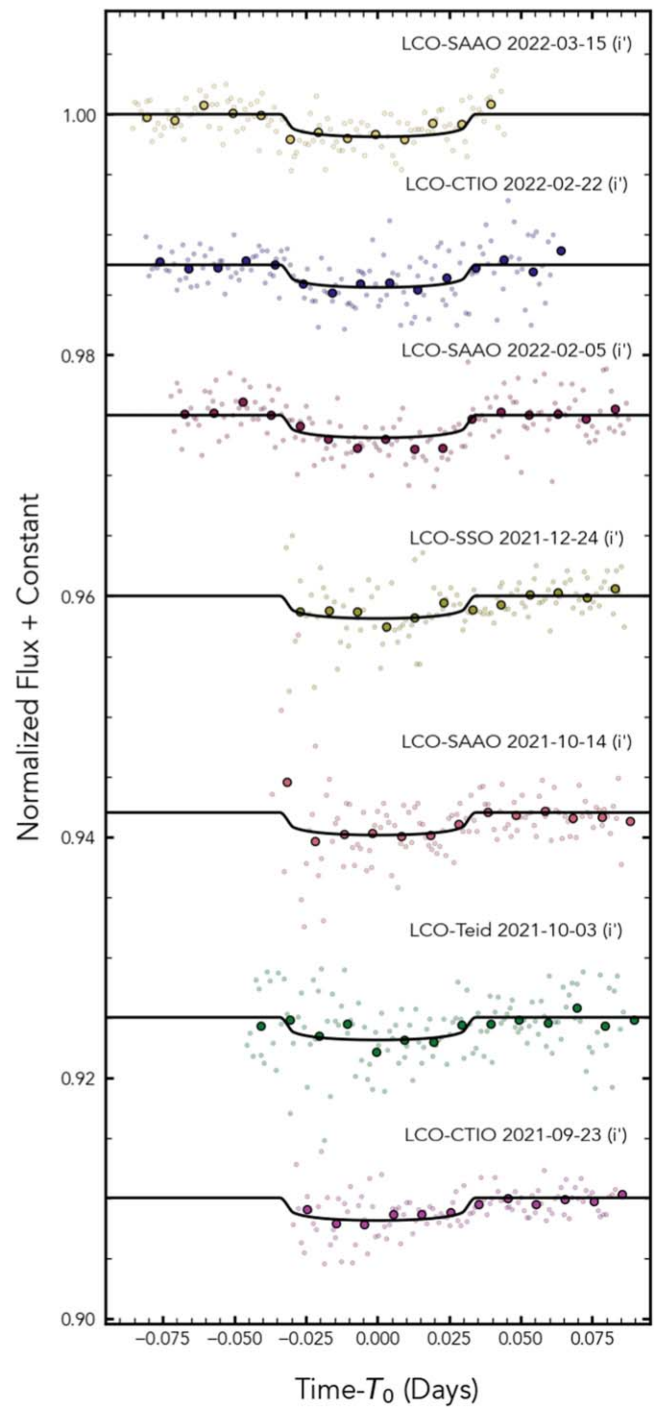

Figure 3. LCOGT 1 m TOI-4364b follow-up observations (small points) along with binned data (larger circles) and best-fit transit models (black line). Individual observations are shifted along the *y*-axis for clarity.

observations taken, with the data shown in Figure 3. All of the follow-up photometry shown is available on ExoFOP (NExScI 2022).[23]

2.3. Radial Velocity Measurements

Several ground-based RV measurements have been collected for our target, along with Gaia DR3 spectra (Gaia Collaboration et al. 2021). The ground-based spectroscopic follow-up

[23] https://exofop.ipac.caltech.edu/tess/target.php?id=4070275

Table 3
Radial Velocity Measurements of TOI-4364

Name	RV (km s^{-1})	Exp. Time (s)	SNR	Time
Gaia DR3[a]	44.77 ± 0.46	⋯	⋯	2016.0
TRES	44.969 ± 0.104	2160	16	2459522.907
TRES	44.980 ± 0.104	2400	15	2459525.825
ESPRESSO	45.087 ± 0.004	1800	15	2459795.889
ESPRESSO	45.108 ± 0.001	1800	34	2459812.881
ESPRESSO	45.103 ± 0.003	1800	21	2459813.828
ESPRESSO	45.109 ± 0.002	1800	29	2459893.824

Note.
[a] Gaia DR3 RV measurements are averaged over multiple visits over 34 months with an average of eight visits per star.

consists of four measurements with the Echelle SPectrograph for Rocky Exoplanets and Stable Spectroscopic Observations (ESPRESSO; F. Pepe et al. 2021), which span over 3 months. It also includes two measurements with the Tillinghast Reflector Echelle Spectrograph (TRES; A. H. Szentgyorgyi & G. Fursz 2007; G. Fűrész 2008), which are separated by 3 days.

The ESPRESSO data were reduced with the Data Reduction Software (DRS) pipeline, which cross-correlates the observed spectrum with a stellar binary mask and then fits the cross-correlation output with a Gaussian to derive the RV. The TRES data were first reduced following the method in L. A. Buchhave et al. (2010). A cross-correlation-function multiorder analysis was then applied to the data to best constrain the RV across the entire spectrum. The precise and stable measurements from TRES and ESPRESSO help to distinguish between planetary signals and potential perturbations caused by unseen stellar companions, with all measurements taken at or near quadrature. We see that the standard deviation of the ESPRESSO data is 9.0 m s^{-1} and the TRES data are separated by 78 m s^{-1}. When we convert the measurements from the two spectrographs to the standard IAU velocity scale, we find that they match at the 220 m s^{-1} level. All of this is consistent with TOI-4364 not being a short-period RV variable. The details of these observations are listed in Table 3.

2.4. High-resolution Speckle Imaging

To investigate potential contamination from stars at small angular separations (possible variables, eclipsing binaries (EBs), or bound companions), we performed high-resolution speckle imaging. By analyzing the speckle data, we can investigate whether the observed transits are influenced by additional "third-light" from close stellar companions. This ensures that the planetary signal remains free from contamination by additional stellar light, which is crucial for accurate characterization and validation of the planet (E. Furlan & S. B. Howell 2017, 2020).

The first Gemini speckle observation for TOI-4364 occurred on 2021 October 16 and was made with the 'Alopeke instrument on Gemini North in Hawaii. The second Gemini observation took place on Gemini South in Chile on 2023 January 5, using the Zorro instrument under conditions of better seeing and offering more time on target. The two instruments are identical, using electron multiplying charge-coupled devices (EMCCDs) to enable fast readout and provide simultaneous two-color imaging (N. J. Scott et al. 2021). Both observations of TOI-4364 were performed using narrowband filters at two separate wavelengths, 832/40 nm and 562/54 nm. This dual-wavelength approach provides a more comprehensive assessment of any detected nearby sources. The speckle data were reduced using our standard pipeline (S. B. Howell et al. 2011). No sources were detected to our magnitude limits, as shown in the top panel of Figure 7.

On 2021 October 18, a broader search for stellar companions was conducted using speckle imaging with the 4.1 m Southern Astrophysical Research (SOAR) telescope (A. Tokovinin 2018). The observation was made in the Cousins *I* band (879 (289) nm), a visible bandpass similar to TESS. Further details about these observations can be found in the SOAR TESS survey (C. Ziegler et al. 2020). No nearby stars were detected within 3″ of TOI-4364 in the SOAR observations, as shown in the bottom panel of Figure 7. Beyond the outer limits of these observations, the Gaia DR3 catalog establishes that there are no neighbors brighter than $G_{\rm Gaia} \approx 21$ mag and within 10″. Further, a search of Gaia DR3 finds that there are no very wide comoving, codistant companions brighter than this magnitude limit out to a projected separation of 1200″ (50,000 au). Therefore, the system does not host any wide binary companions that might induce long-term dynamical evolution of the planetary system.

3. Analysis

To optimally characterize the star–planet system, we leveraged the properties that TOI-4364 shares with the Hyades to then perform a global analysis of the star–planet system.

3.1. Association of TOI-4364 with the Hyades Cluster

Galactic space velocity values were calculated using `PyAstronomy` tools, following the methodology outlined in D. R. H. Johnson & D. R. Soderblom (1987) and utilizing data from Gaia DR3. The spatial center of the Hyades cluster is (−44.77, +0.40, −16.24) pc (S. Röser et al. 2019). This can be compared to the Cartesian Galactic coordinates of TOI-4364, measured as (−36.47, −17.86, −16.56) pc. TOI-4364 is approximately 20.1 pc from the core of the Hyades cluster. Previous works have shown that the Hyades exhibits a dispersed structure, including extensive tidal tails that span over 100 pc in size (S. Rser et al. 2019). 3D kinematic modeling has confirmed that TOI-4364 is a high-confidence member of the Hyades, with a membership probability exceeding 99% (S. Oh & N. W. Evans 2020). The location of TOI-4364 within the tidal tail (S. Rser et al. 2019) accounts for its distance relative to the core members of the Hyades (N. Lodieu et al. 2019).

To establish when TOI-4364 last interacted with the core of the Hyades, we performed a series of simulations using the `galpy` module (J. Bovy 2015). We used the positions stated above for both the Hyades and TOI-4364, using the Gaia proper motions and our new RV measurement as velocity inputs for TOI-4364, and using the mean proper motions and RVs for the Hyades presented by D. R. Ciardi et al. (2018) and Y. Tarricq et al. (2021), respectively. We then Monte Carlo sampled the velocities of both the Hyades and TOI-4364 according to their uncertainties and simulated the positions of the samples back 700 Myr through all 10 potentials available through `galpy` (W. Dehnen & J. Binney 1998; A. Irrgang et al. 2013; J. Bovy 2015; P. J. McMillan 2017; M. Cautun

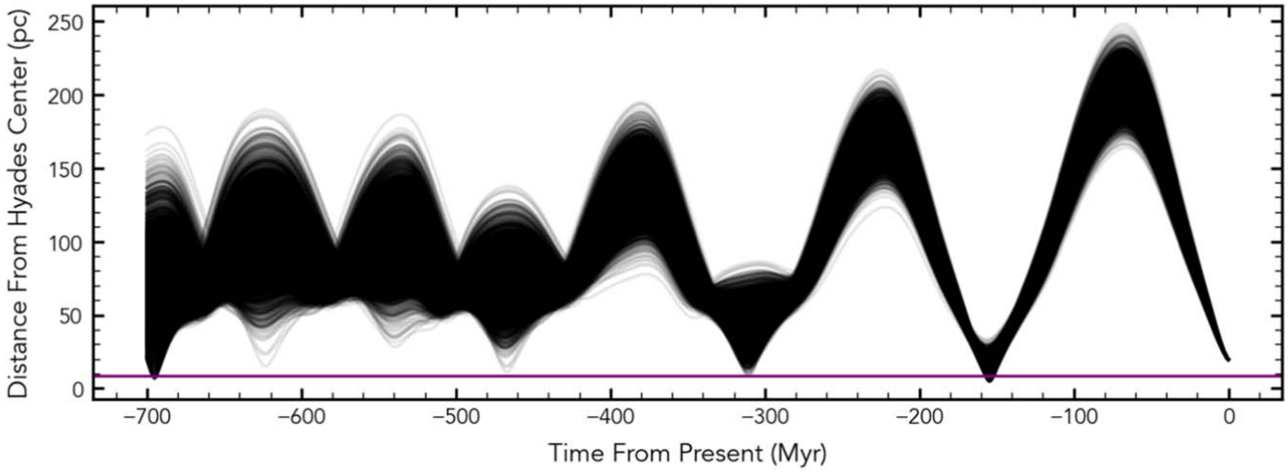

Figure 4. TOI-4364's distance from the Hyades center over the course of the cluster's lifetime. Each curve shows one simulation with the current position and velocity varied within its uncertainties and traced back through the `MWPotential2014` galactic potential (J. Bovy 2015) over the past 700 Myr. The most recent potential pass within the Hyades cluster's tidal radius was 155 Myr ago, which is a plausible ejection time.

et al. 2020). We used 1000 Monte Carlo samples for all potentials except `MWPotential2014`, where we used 5000 samples.

All simulations (displayed in Figure 4) show that TOI-4364 has been getting closer to the Hyades for about the past 70 Myr, which is supported by its velocity oriented slightly toward the Hyades. However, all simulations also show a local minimum at 155 Myr, and 21% of simulations using `MWPotential2014` see TOI-4364 come within the 9 pc tidal radius of the Hyades 155 Myr ago. `MWPotential2014` also shows a minimum 310 Myr ago, while the `McMillan17`, `Cautun20`, and A. Irrgang et al. (2013) potentials highlight a minimum at 436 Myr. However, on timescales of hundreds of megayears, traceback simulations become increasingly unreliable owing to uncorrected gravitational interactions, making 9 pc precision increasingly implausible. Therefore, while we cannot conclusively determine when TOI-4364 was ejected from the Hyades, our simulations determine that TOI-4364 has been beyond the tidal radius of the Hyades for at least the past 150 Myr. 155 Myr ago represents a plausible recent ejection time, although we cannot exclude several earlier times.

3.2. TOI-4364 Photometric Rotation Period

To accurately determine the photometric rotation period of TOI-4364, we analyzed the processed TESS data, as described in Section 2. The data were binned to 30 minutes to reduce scatter, better capturing longer-period stellar rotation signals. We also removed contaminated parts of the light curve, which included the initial 0.2 days of Sector 5 and the first 0.2 days after the downlink of Sector 32.

Our Lomb−Scargle periodogram (N. R. Lomb 1976; J. D. Scargle 1982) and autocorrelation function analysis suggested a photometric rotation rate of approximately 5 days. However, under more scrutiny, we observed recurring substructure in the light curve indicating a ~10-day rotation period. This recurring substructure is illustrated in the top left and right panels of Figure 5.

To optimally characterize this structure, we employed a phase dispersion minimization (PDM) algorithm from the package `starrotate`[24](R. Angus & A. Garcia Soto 2023). The PDM algorithm detects periodic signals in unevenly sampled data by folding them over trial periods and minimizing the scatter within phase bins (described further in R. F. Stellingwerf 1978). The θ value reflects the scatter on the folded data, with values closer to 0 having less scatter and values closer to 1 having more scatter.

The photometric rotation period is dependent on the presence of spots, spot latitude, and the strength of differential surface rotation. We measured a period of 10.51 days for Sector 5 and 10.63 days for Sector 32. The PDM output and corresponding phase-folded light curves are shown in Figure 5.

Stellar rotation offers a method to estimate a cluster's age. A. Skumanich (1972) showed that average stellar rotational velocity decreases with cluster age. For low-mass stars, this decline is driven by magnetic braking, where the star's magnetic field interacts with outflowing charged particles, removing angular momentum and slowing rotation over time (L. Mestel 1968; S. Gossage et al. 2023).

Consequently, the rotational sequence of a cluster can be compared with those of other clusters to estimate its age. Figure 6 illustrates the rotation sequence for the Hyades alongside the Pleiades (120 Myr), Praesepe (670 Myr), and NGC 6811 (1 Gyr). The rotational sequence of the Hyades exhibits a slope comparable to that of Praesepe (S. Gossage et al. 2018), thus supporting the `EXOFASTv2` age estimate of 710 ± 100 Myr. Note that M dwarfs, like our planet host TOI-4364, exhibit a wide dispersion of rotation periods.

3.3. EXOFASTv2 Analysis

To determine the best-fit transit parameters, our team constructed a global fit from the `EXOFASTv2`[25] (J. Eastman et al. 2013; J. D. Eastman et al. 2019) software package. `EXOFASTv2` utilizes a differential evolution Markov Chain Monte Carlo (MCMC) approach to fit both planetary and stellar parameters within a system simultaneously. This allowed us to jointly model the star's spectral energy distribution (SED) using `PARSEC` (A. Bressan et al. 2012) in parallel with TESS and follow-up transit observations of the planet, thereby ensuring consistency across the data. `PARSEC` isochrones were chosen

[24] https://github.com/RuthAngus/starrotate

[25] https://github.com/jdeast/EXOFASTv2

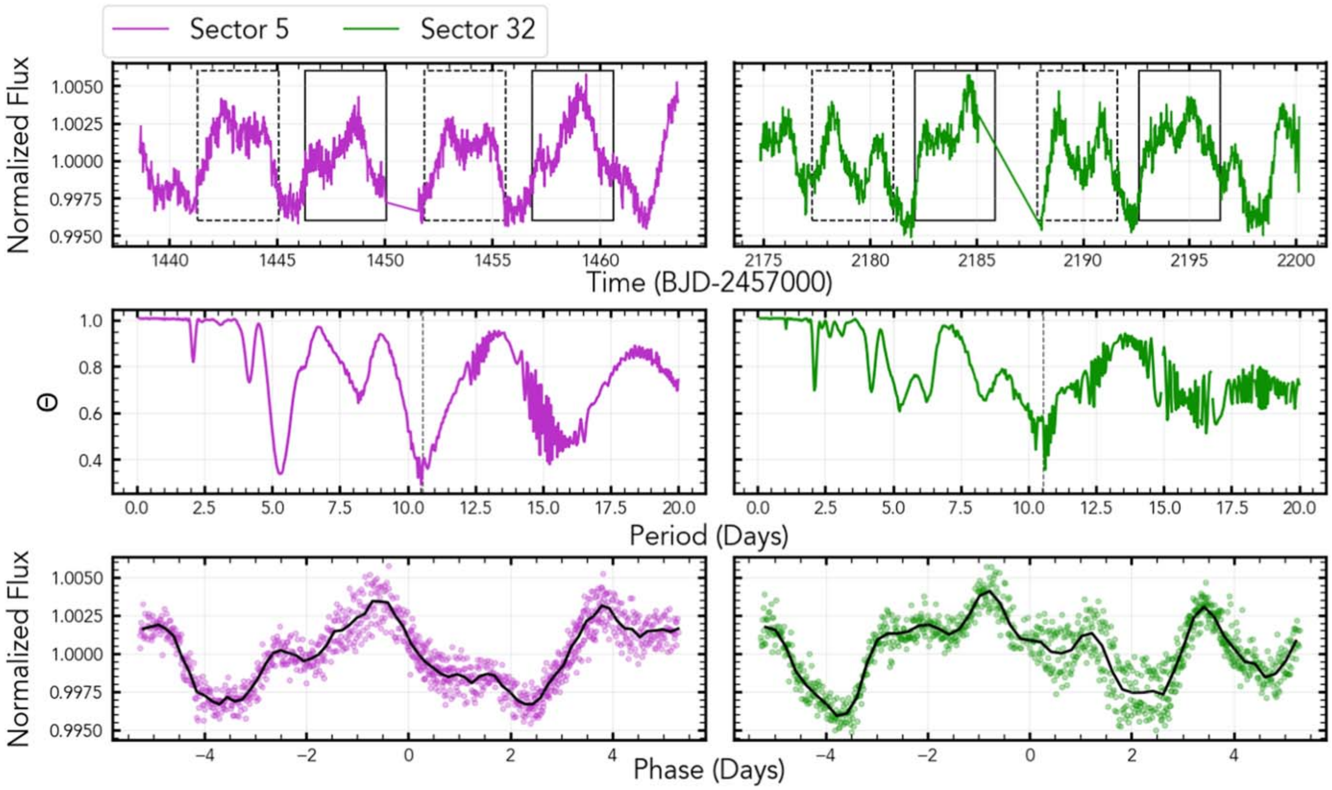

Figure 5. Analysis of TOI-4364's photometric rotation period using TESS Sectors 5 (purple) and 32 (green). Top: trimmed light curve with boxes showing similar structures; middle: PSM output, with maximum likely periods shown with dashed lines; bottom: phase-folded light curves for each sector at $P = 10.57$ days.

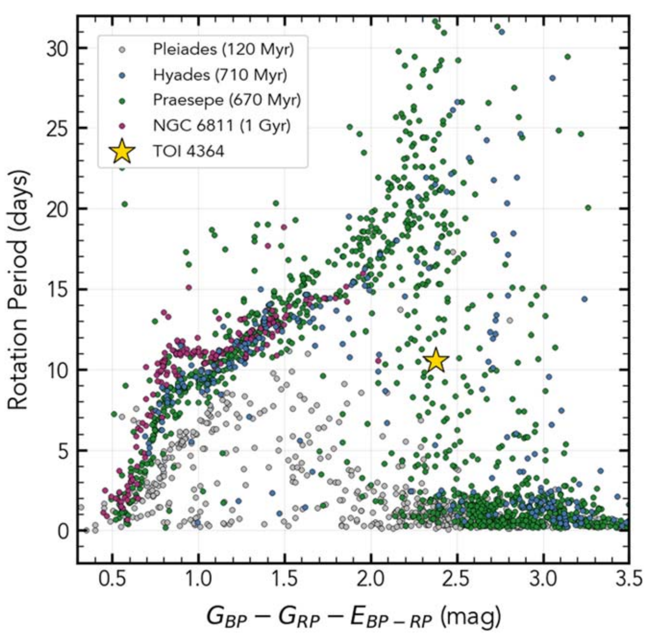

Figure 6. The color−rotation sequence for catalog members of the Hyades cluster, as compared to the Pleiades (120 Myr; L. M. Rebull et al. 2016), Praesepe (670 Myr; S. T. Douglas et al. 2017), and NGC 6811 (1 Gyr; J. L. Curtis et al. 2019). TOI-4364 is depicted as a gold star.

owing to their accuracy in matching observations in the $G_{Bp} - G_{Rp}$ regime of TOI-4364.

To construct the SED, we gathered archival photometric data from several sources: Gaia DR3 (Gaia Collaboration et al. 2016, 2021), the Two Micron All Sky Survey (2MASS; R. M. Cutri et al. 2003), and the Wide-field Infrared Survey Explorer (WISE; E. L. Wright et al. 2010; R. M. Cutri et al. 2012). To set an upper bound for the visual extinction, we used the Bayestar 3D dust maps (G. M. Green et al. 2015; G. Green 2018; G. M. Green et al. 2019) and calculated a value of $A_V = 0$. To account for this in the EXOFASTv2 analysis, we then set an upper bound of $A_V < 0.001$. In regard to previous estimates for the Hyades (see W. Brandner et al. 2023 for a summary), we opted to adopt a broad Gaussian prior for the age of TOI-4364 of 700 ± 100 Myr and a metallicity of $[\mathrm{Fe/H}] = 0.155 \pm 0.095$ dex.

The planetary parameters are predominately constrained by the transit light curves listed in Tables 1–2. The TESS light curves were processed using the method discussed in Section 2.1. They were then flattened using keplersplinev2,[26] a Python-based spline fitting tool. The spline break-point spacing was chosen as the value that minimizes the Bayesian information criterion. The TESS light curves were then truncated to remove unnecessary out-of-transit data, retaining a baseline of one transit duration on either side of each transit. The follow-up light curves were flattened using AstroImageJ (K. A. Collins et al. 2017). No prior estimate was placed on the linear and quadratic limb-darkening coefficients, which were allowed to vary as free parameters. To estimate the mass of the planet, EXOFASTv2 uses the mass–radius relation from J. Chen & D. Kipping (2017).

We followed the default EXOFASTv2 MCMC setup, with twice as many chains as the number of parameters in each fit. For the circular fit, this meant 46 parameters and 92 chains. For

[26] https://github.com/avanderburg/keplersplinev2

Table 4
Stellar Properties of TOI-4364

Parameter	Value	Source
TIC ID	4070275	TESS Input Catalog
Gaia DR3 ID	3210444215030339584	Gaia DR3
	Astrometry	
α.	80.067 ± 0.014	Gaia DR3
δ.	− 4.239 ± 0.011	Gaia DR3
μ_α (mas yr^{-1})	64.456 ± 0.017	Gaia DR3
μ_δ (mas yr^{-1})	43.789 ± 0.014	Gaia DR3
π (mas)	22.805 ± 0.012	Gaia DR3
Distance (pc)	43.85 ± 0.04	Gaia DR3
	Photometry	
Spectral type	M4V	This paper
$G_{\rm Gaia}$ (mag)	12.534 ± 0.006	Gaia DR3
$G_{\rm BP}$ (mag)	13.796 ± 0.033	Gaia DR3
$G_{\rm RP}$ (mag)	11.420 ± 0.012	Gaia DR3
V (mag)	13.56 ± 0.03	N. Zacharias et al. (2013)
J (mag)	9.952 ± 0.024	2MASS
H (mag)	9.307 ± 0.022	2MASS
Ks (mag)	9.075 ± 0.024	2MASS
W1 (mag)	8.949 ± 0.023	ALLWISE
W2 (mag)	8.857 ± 0.02	ALLWISE
W3 (mag)	8.764 ± 0.03	ALLWISE
W4 (mag)	8.833 ± 0.438	ALLWISE
A_V (mag)	0.00050 ± 0.00034	This paper*
	Kinematics and Galactic Position	
RV$_{\rm Bary}$ (km s^{-1})	44.770 ± 0.455	Gaia DR3
U (km s^{-1})	− 43.505 ± 0.047	This paper
V (km s^{-1})	−19.235 ± 0.018	This paper
W (km s^{-1})	−2.002 ± 0.015	This paper
X (pc)	−36.469 ± 0.039	This paper
Y (pc)	−17.855 ± 0.016	This paper
Z (pc)	−16.555 ± 0.003	This paper
	Physical Properties	
$P_{\rm rot}$ (days)	10.57 ± 0.06	This paper
Age (Myr)	710 ± 100	This paper*
$T_{\rm eff}$ (K)	3528^{+33}_{-20}	This paper*
$M_\star$ ($M_\odot$)	$0.487^{+0.017}_{-0.016}$	This paper*
$R_\star$ ($R_\odot$)	$0.4684^{+0.0087}_{-0.010}$	This paper*
$L_\star$ ($L_\odot$)	$0.03075^{+0.00085}_{-0.00084}$	This paper*
L_X (erg s^{-1})	2.07×10^{28}	S. Freund et al. (2020)
$\rho_\star$ (g cm^{-3})	$6.69^{+0.38}_{-0.33}$	This paper*
log(g) (log(cm/s^2))	$4.785^{+0.017}_{-0.016}$	This paper*
[Fe/H] (dex)	0.148 ± 0.046	This paper*

Note. Values marked with an asterisk were obtained from EXOFASTv2.

the fit where eccentricity was allowed to float, there were 50 parameters and 100 chains. To ensure robust and converged results, we implemented strict convergence criteria, requiring a Gelman–Rubin statistic (A. Gelman & D. B. Rubin 1992) less than 1.01 and more than 1000 independent draws. The Gelman–Rubin statistic criterion is typically the more difficult to reach. In the case of the eccentric fit, the MCMC had a Gelman–Rubin statistic of 1.0084 and 5783 independent draws after accepting 9.26% of the total number of steps. Our EXOFASTv2 MCMC circular fit resulted in a Gelman–Rubin statistic of 1.0041 and 4727 independent draws after accepting 17.02% of the total number of steps. The resulting stellar parameters are provided in Table 4. The orbital fit parameters are provided in Table 5. The best-fit models are illustrated in Figures 1–3.

Table 5
Transit Fit Parameters for TOI-4364b

Parameter	Value e Free	Value $e = 0$
P (days)	$5.424019^{+0.000010}_{-0.000011}$	5.424019 ± 0.000011
T_0 (BJD)	2458439.3428 ± 0.0020	2458439.3431 ± 0.0020
$a/R_\star$	$21.83^{+0.41}_{-0.36}$	$21.86^{+0.41}_{-0.36}$
i (deg)	$88.68^{+0.85}_{-0.40}$	$88.46^{+0.11}_{-0.10}$
e	$0.29^{+0.38}_{-0.17}$	0
$\omega_\star$ (deg)	-190^{+160}_{-130}	0
u_1 (TESS)	0.312 ± 0.036	0.287 ± 0.036
u_2 (TESS)	0.34 ± 0.036	$0.360^{+0.036}_{-0.035}$
u_1 (i')	0.341 ± 0.021	$0.316^{+0.019}_{-0.020}$
u_2 (i')	$0.315^{+0.020}_{-0.021}$	0.336 ± 0.019
$R_p/R_\star$	$0.0394^{+0.0017}_{-0.0014}$	$0.0402^{+0.0012}_{-0.0013}$
$\delta_{\rm TESS}$	0.00178 ± 0.00010	0.00175 ± 0.00010
$\delta_{i'}$	0.00179 ± 0.00010	0.00180 ± 0.00010
t_{14} (days)	$0.0668^{+0.0020}_{-0.0015}$	$0.0677^{+0.0014}_{-0.0013}$
t_{12} (days)	$0.00298^{+0.0013}_{-0.00047}$	$0.00393^{+0.00023}_{-0.00022}$
	Derived Parameters	
R_p ($R_\oplus$)	$2.01^{+0.10}_{-0.08}$ $R_\oplus$	$2.05^{+0.08}_{-0.08}$
a (au)	$0.04753^{+0.00053}_{-0.00054}$	0.04753 ± 0.00053
$T_{\rm eq}$ (K)	488^{+9}_{-7}	534.4 ± 3.9
TSM	44.2	45.1
ESM	4.9	5.1

Note. Top: transit fits obtained from the joint SED, TESS, and follow-up photometry using the EXOFASTv2 model. Bottom: derived system parameters. The middle column presents the results when the eccentricity (e) and argument of periapsis (ω) are allowed to vary as free parameters. The rightmost column shows the fit assuming $e = 0$ and $\omega = 0$.

4. Ruling Out False-positive Scenarios

4.1. Possible False-positive Scenarios

In our efforts to validate the detection of TOI-4364b, we utilized LEO-vetter,[27] an automated tool designed to assess potential exoplanet signals in light-curve data. TOI-4364b successfully passed all assessments conducted by LEO-vetter, including flux and pixel vetting analyses. These tests examined the transit shape to exclude EBs and analyzed centroid offsets to confirm the accuracy of the transit event locations.

Given the absence of additional validation methods for TOI-4364b, we worked to exclude all plausible false-positive scenarios, as detailed below.

1. Instrumental Artifacts and Stellar Variability: No instrumental artifacts in the TOI-4364 TESS light curves have been identified that could replicate the observed signal in the BLS periodogram. Furthermore, the transit signal has been independently verified photometrically by observations from four separate facilities, eliminating the likelihood of an instrumental artifact. While M dwarfs are known for their significant variability (L. Mignon et al. 2023), particularly those younger than 1 Gyr, no known phenomenon could induce a transit-like flux dip that recurs consistently over multiple years. Stellar variability typically manifests as gradual changes over days, weeks, or months, rather than the distinct transit-like flux dips observed.

[27] https://ascl.net/2404.026

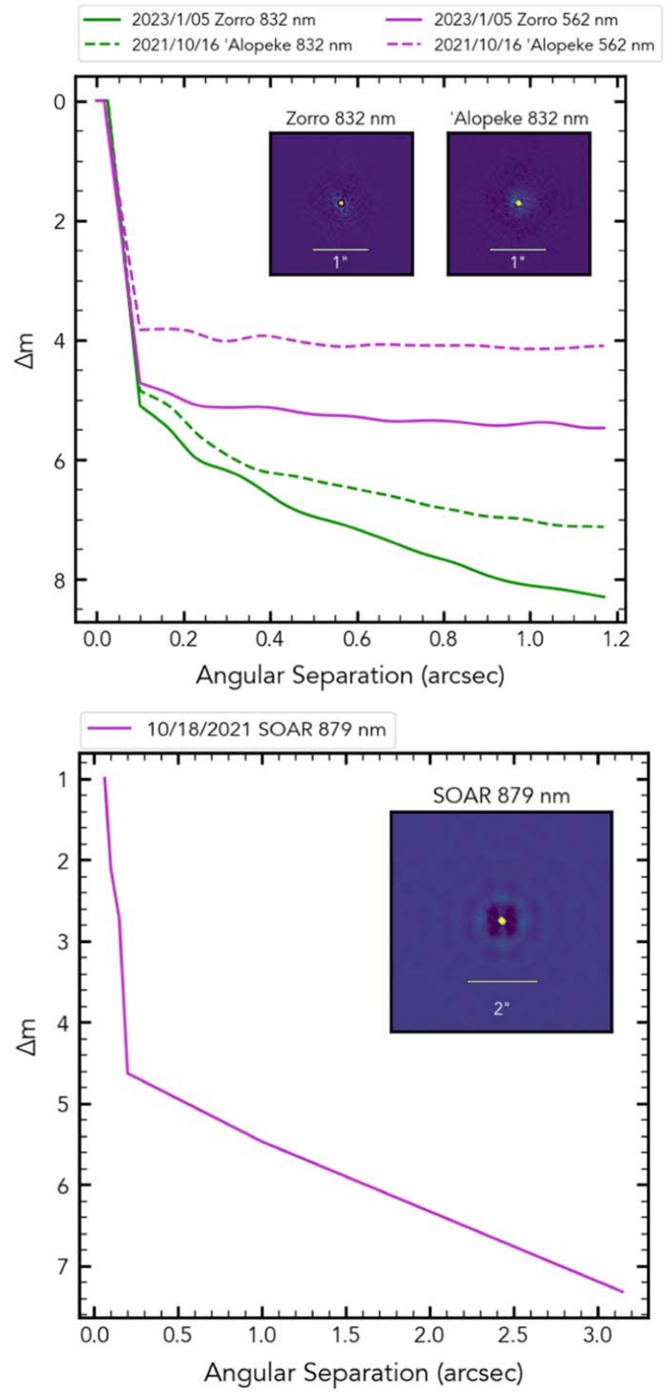

Figure 7. Top panel: contrast curves obtained from Gemini North 'Alopeke and Gemini South Zorro instruments. Insets showcase 832 nm reconstructed images, highlighting the increased contrasts achieved with Zorro on Gemini South due to better seeing conditions and a longer total integration time. No close companion star was detected within the achieved 5σ magnitude contrast curves and angular limits from the 8 m diffraction limit out to $1\overset{''}{.}2$. At the distance of TOI-4364, these limits correspond to spatial separations ranging from 0.88 to 52.8 au. Bottom panel: SOAR sensitivity curve taken on 2021 October 18. The 5σ sensitivity limits are shown out to $3\overset{''}{.}15$, corresponding to a projected separation of 138.1 au.

2. Target Is an EB: A possible concern is that the target star might be an EB. However, if this were the case, one would expect large-scale RV variations on the order of kilometers per second, as the companion would need to have an inclination of near 90° to produce a transit-like signal. Instead, the TRES data reveal a maximum spread between RVs to be 78 m s^{-1} (taken at opposite quadratures), indicating that TOI-4364 is not an EB in a 5.42-day orbit.
3. Contamination by Foreground or Background EBs: Another potential false-positive scenario is the presence of an EB in the foreground or background of the target, which would not have an effect on the RV measurements of TOI-4364. Given the large pixel scale of TESS, this is an important consideration. The required magnitude difference of a contaminating EB is given by

$$\Delta m \lesssim 2.5 \log_{10}\left(\frac{t_{12}^2}{t_{13}^2 \delta}\right), \tag{1}$$

where δ is the transit depth, t_{12} is the ingress duration, t_{14} is the full transit duration, and $t_{13} = t_{14} - t_{12}$ (A. Vanderburg et al. 2019). To calculate this magnitude difference, our team employed the differential MCMC code `edmcmc`[28] coupled with `batman`[29] to optimally constrain the orbital parameters. We employed the data, as described in Section 2.1, removing observations that were not within ±0.1 days of the transit (as predicted by `EXOFASTv2`). We ran the code with 50 walkers for 10,000 links, with 4000 burn-in links. We fixed the eccentricity to zero and argument of periapsis to 90° and used a prior of the `EXOFASTv2` output for the walkers. All orbital parameters were run to a Gelmin–Rubin statistic of <1.05. Following this analysis, we arrive at a limiting contaminating EB magnitude of $\Delta m \leqslant 3.65$ mag at 95% confidence. The 832 nm Zorro speckle imaging contrast curves in the top panel of Figure 7 illustrate a 3.87 mag contrast at $0\overset{''}{.}085$, which corresponds to a projected separation of 3.73 au. For the outer limit, the 879 nm SOAR imaging observation (bottom panel of Figure 7) also confirmed the lack of an object bright enough to cause this signal out to 3″. Although this is within the follow-up photometric radius, a 15.04 TESS magnitude star would be clearly resolved by Gaia given a contrast sensitivity above 99% for $\Delta G_{\rm Gaia} < 6$ mag (A. Brandeker & G. Cataldi 2019). Given that the follow-up photometry constrained the signal to be within $4\overset{''}{.}0$ of TOI-4364, it is very unlikely that the signal comes from a contaminating EB.
4. Physically Associated EBs: Another possibility is that TOI-4364 has a physically associated EB companion that could account for the observed signal. This cannot be completely ruled out, as the angular separation may be small enough that it is unresolved by the speckle imaging. In such a case, the inclination would need to be near 0° to prevent a significant RV shift in TOI-4364. This is unlikely for several reasons. First, it is statistically unlikely given that M dwarfs have a very low triple rate of ≈3.3% (J. G. Winters et al. 2019)). Second, the Zorro contrast curve rules out the presence of companions bright enough to induce this signal at distances beyond 3.73 au (corresponding to a maximum period of 10.3 yr). Given the maximum ESPRESSO RV shift of 28 m s^{-1}

[28] https://github.com/avanderburg/edmcmc
[29] https://lkreidberg.github.io/batman/docs/html/index.html

Table 6
Planets in the Hyades

Planet	Period (days)	Radius ($R_\oplus$)	Mass ($M_\oplus$)	Distance[a] (pc)	V (mag)	References
TOI-4364b	5.4	2.0 ± 0.1	⋯	43.9	13.6	This paper
K2-25 b	3.5	3.4 ± 0.1	24.5 ± 6	44.7	15.9	G. Stefansson et al. (2020)
HD 285507b	6.1	⋯	292 ± 10.5[b]	45.0	10.5	S. N. Quinn et al. (2014)
K2-136 b	8.0	1.0 ± 0.1	<2.9	58.9	11.2	A. W. Mayo et al. (2023)
K2-136 c	17.3	3.0 ± 0.1	18.1 ± 2.0	58.9	11.2	A. W. Mayo et al. (2023)
K2-136 d	25.6	1.5 ± 0.1	<1.3	58.9	11.2	A. W. Mayo et al. (2023)
HD 283869b	106.0	2.0 ± 0.2	⋯	47.4	10.6	A. Vanderburg et al. (2018)
HD 28305b	585.8	⋯	2285.7 ± 17.8[b]	44.7	3.5	H. Y. Teng et al. (2023)

Notes. The errors are reported to 68% confidence.
[a] Distances are obtained with Gaia DR3.
[b] $M \sin(i)$.

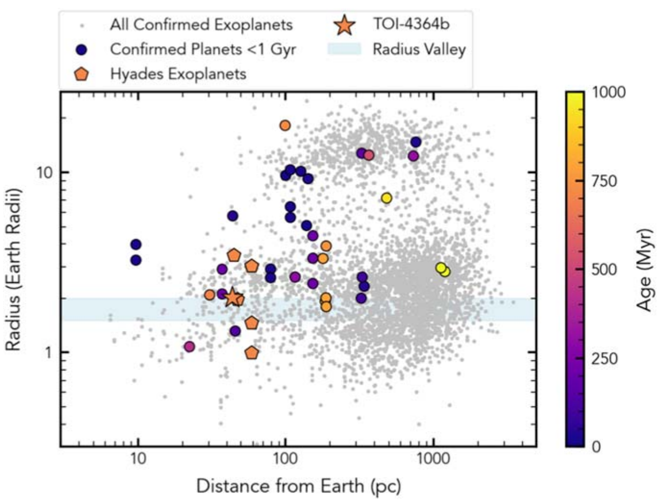

Figure 8. Distance from Earth vs. planet radius for confirmed exoplanets (gray circles), young (<1 Gyr) planets with well-constrained ages (colored circles), previously discovered Hyades exoplanets (pentagons), and TOI-4364b (star). TOI-4364b stands out as a nearby young planet at the upper edge of the radius valley, making it a prime target for atmospheric and evolutionary studies.

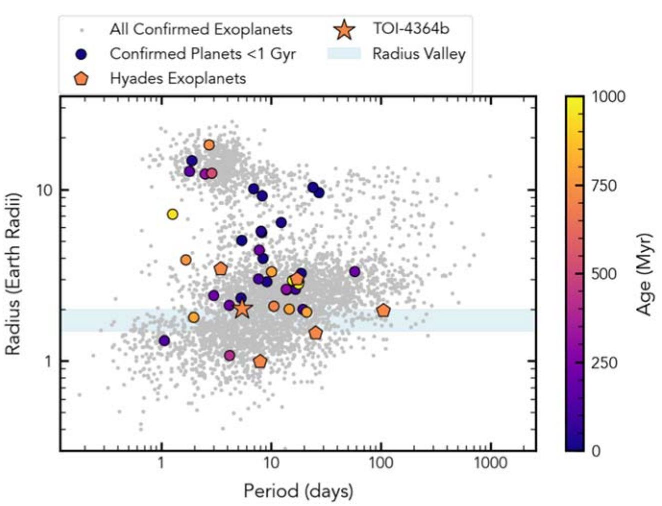

Figure 9. Period–radius distribution of confirmed exoplanets (gray circles), confirmed young (<1 Gyr) exoplanets with well-constrained ages (colored circles), previously discovered Hyades exoplanets (pentagons), and TOI-4364b (star). To enhance the readability of the figure, we omit planets discovered via direct imaging. Note that TOI-4364b resides at the upper edge of the radius valley (blue strip).

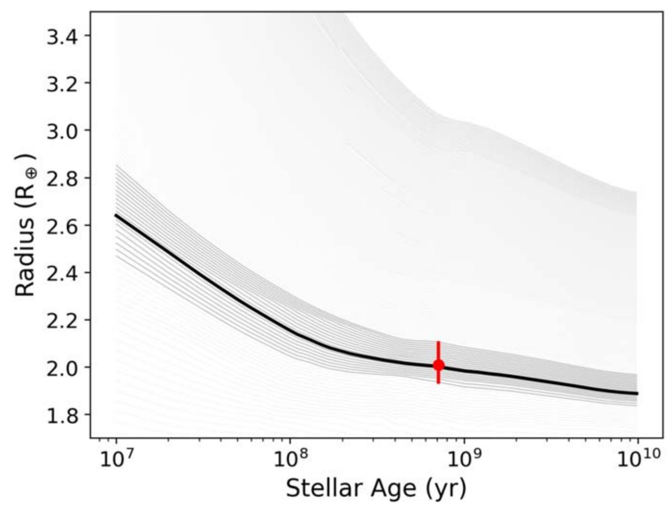

Figure 10. Evolution of the planetary radius as a function of stellar age for TOI-4364b, assuming the best-fit planetary parameters (including planetary mass). The gray and black lines represent the radius evolution predicted by the `VPLanet` model, which incorporates both planetary cooling and photoevaporation effects. Each line corresponds to a different initial H/He envelope fraction, ranging from 0% to 10%. The red circle marks the observed planetary radius at 710 Myr, with error bars indicating the 1σ uncertainty. The darker contour lines show models that are consistent with the observed radius, which have H/He envelope fractions between 0.4% and 0.9%. The nominal best-fit solution is shown as a thicker line, which corresponds to a current-day envelope fraction of 0.6%. Over time, the planet's radius is expected to decrease gradually owing to continued cooling and mass loss from photoevaporation.

(taken over 3 months), a companion would need to have an extremely low inclination. While there is no way to completely rule out this scenario, it is unlikely that a bound EB is producing the transit signal of TOI-4364b.

4.2. Statistical Validation with TRICERATOPS

To further validate our conclusion that no false-positive scenarios could mimic the signal of TOI-4364b, we employed the TRICERATOPS pipeline (S. Giacalone et al. 2021) to assess the likelihood of various false-positive scenarios. TRICERATOPS utilizes Bayesian inference to compute the probability that an input light curve originates from a wide range of scenarios. This includes assessing the shape of the

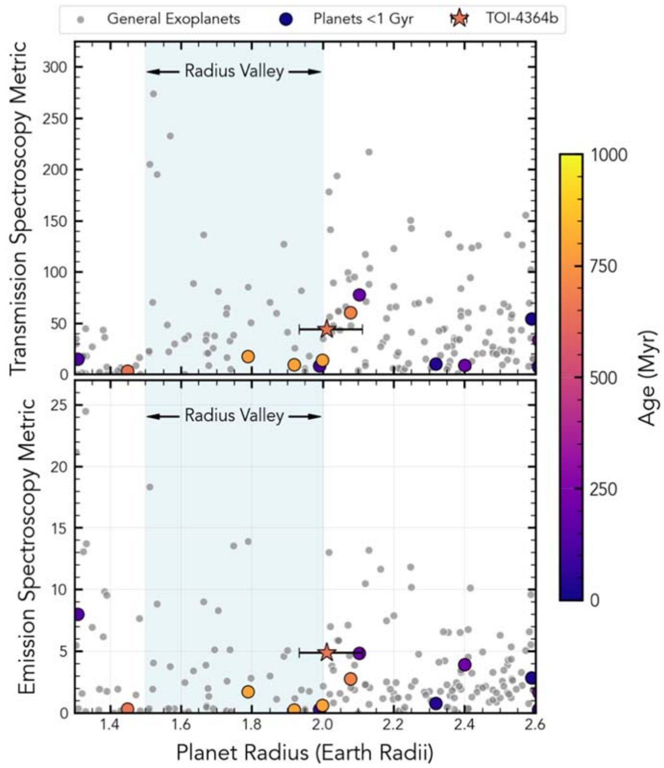

Figure 11. TSM (top panel) and ESM (bottom panel) values as a function of planet radius for TOI-4364b (star), the population of confirmed exoplanets (gray circles), and young planets with well-constrained ages (<1 Gyr; larger circles). The blue shaded region indicates the location of the radius valley as in B. J. Fulton et al. (2017).

transit signature and conducting checks for instrumental artifacts or background contamination.

We ran TRICERATOPS 20 times using data from the contrast curves obtained by the Zorro speckle imaging. Each run included 10^6 instances, which yielded a false-positive probability—the likelihood that the transit signal is not due to a planet—of 0.00319 ± 0.00017. Similarly, the nearby false-positive probability—the likelihood that the transit signal is due to a nearby object—was found to be 0.00317 ± 0.00017. These low false-alarm probabilities allow us to statistically confirm that TOI-4364b is indeed a planet. Moreover, while the false-alarm probabilities are low, they likely overestimate the true values since existing follow-up photometry using smaller apertures could not be included. From this analysis, we conclude that TOI-4364b is a genuine exoplanet.

5. Discussion

5.1. TOI-4364b in Context

TOI-4364b serves as a key benchmark for studying exoplanets within the Hyades cluster, which is known to host eight planets. Table 6 presents a comparison of TOI-4364b's properties with those of the other Hyades planets. Notably, TOI-4364b has the second-shortest orbital period among them. Further, its location near the upper boundary of the radius valley makes it a particularly valuable target for probing planetary evolution. Given its youth and proximity, TOI-4364b offers an invaluable opportunity to investigate how planetary radii evolve as a function of system age.

When compared to the broader population of confirmed[30] exoplanets, as shown in Figure 8, TOI-4364b continues to stand out for its proximity to Earth. This is especially significant when considering planets younger than 1 Gyr with well-constrained ages. For clarity, we define a "well-constrained" age as one where both the upper and lower error is at most 20% of the estimated value. The apparent brightness of TOI-4364b makes it an exceptional target for studying planetary evolution among M dwarf planetary companions. Precise age constraints for M dwarf planets are often lacking owing to the host stars' low luminosity and the challenges associated with dating these slowly evolving stars. The proximity of TOI-4364b, combined with its well-constrained age, provides a rare opportunity to address this gap, offering critical insights into how planets form, migrate, and evolve around low-mass stars.

Figure 9 illustrates the period–radius diagram, highlighting young objects with precisely measured age estimates, including TOI-4364b and other known Hyades exoplanets. Even among young systems, TOI-4364b currently resides at a critical boundary of the radius valley.

5.2. Evolving Physical and Orbital Properties

Comparisons to older planets and broader planet samples must be contextualized with the ongoing evolutionary changes that are relevant to a young planet like TOI-4364b. In the following subsections, we discuss some of these considerations.

5.2.1. Planetary Radius

The measured radius of TOI-4364b of $2.01^{+0.10}_{-0.08}\ R_{\oplus}$ places it just above the threshold where a planet is expected to possess an H/He envelope (E. D. Lopez & J. J. Fortney 2014; L. A. Rogers 2015). Yet, given the young age of this planet, it is important to note that the radius is likely to change with time, due to both cooling of the planetary core (which releases energy to the atmosphere and leads to higher envelope entropy at earlier times) and photoevaporation from the insolation by the host star (which leads to a mass outflow from the planet's atmosphere, decreasing the envelope mass over time). Younger planets will retain higher levels of envelope entropy, and as planets with H/He envelopes are irradiated by their host stars, they will also lose mass owing to photoevaporation. This mass-loss rate (A. J. Watson et al. 1981; E. D. Lopez et al. 2012; R. Luger & R. Barnes 2015; R. Barnes et al. 2020) can be modeled as

$$\dot{m} = \epsilon\left(\frac{{R_p}^3 L_{\rm XUV}}{4Ka^2 G M_p}\right), \quad (2)$$

where $\epsilon = 0.1$ is the heating efficiency, R_p is the radius of the planet, $L_{\rm XUV}$ is the X-ray and ultraviolet (XUV) luminosity of the host star, K is the tidal enhancement factor (N. V. Erkaev et al. 2007), a is the semimajor axis, G is the gravitational constant, and M_p is the mass of the planet (predicted from J. Chen & D. Kipping 2017 to be $5.3^{+1.9}_{-1.2}\ M_{\oplus}$). We assume that the planetary atmosphere becomes optically thick to XUV photons at $1R_p$. In the subsequent analysis, we set all planetary

[30] Confirmed exoplanets have been verified through multiple independent methods or extensive observations.

parameters to be their best-fit values given in Table 5 for the free-eccentricity solution and assume a stellar mass of 0.49 $M_{\odot}$.

To evaluate the radius evolution of TOI-4364b, we ran a series of models using the code `VPLanet` (R. Barnes et al. 2020) and its `AtmEsc` and `STELLAR` modules. `VPLanet` allows us to integrate the effects of photoevaporation and planetary cooling to simulate the evolution of a planet's radius as a function of stellar age, planet mass, and envelope fraction. In our models, we use interpolated stellar luminosity tracks from I. Baraffe et al. (2015) and the mass–radius model from E. D. Lopez et al. (2012). Our simulations assume that photoevaporation begins after disk dissipation at approximately 10 Myr.

In the first set of simulations, we set the planet mass to the predicted mass from J. Chen & D. Kipping (2017), running 300 simulations with initial H/He envelope mass fraction varying between 0% and 10%. The results of these simulations are shown in Figure 10, which depicts the computed evolution for each of our 300 grid points. For comparison to the models, the current-day measured radius of TOI-4364b is denoted by a red circle, with error bars denoting the 1σ uncertainty. Models consistent with the observed radius of TOI-4364b are denoted by darker, thicker lines, with the nominal best-fit solution shown by the largest line width. Models consistent with the observed radius at 710 Myr correspond to current H/He envelope fraction ranging between 0.4% and 0.9%. This corresponds to an initial H/He envelope mass fraction range of 0.8%–1.4%. The best-fit solution suggests an initial envelope fraction of 1.0%, which, after accounting for the aforementioned evolutionary processes, results in a current H/He envelope fraction of 0.6%. Over the next few gigayears, the predicted radius evolution for these allowed solutions is minimal, with a maximal 10% decrease.

We ran a second set of simulations to assess the impact of the uncertainty of the planetary mass on the computed allowable envelope fractions. In the second set of simulations, we varied both the planet's mass (within the 1σ range) and its initial envelope fraction, with a total of 20 grid points in each dimension for a total of 400 simulations. This resulted in a broader range of viable initial H/He envelope mass fractions. These span between 0.5% and 1.8%, with current envelope mass fractions ranging between 0.4% and 1%. In this case, the predicted radius evolution is more substantial, with the planet's radius potentially decreasing by up to 15% over the next few gigayears. We note that these envelope fractions assume that the planet's true mass lies within the 1σ range given by J. Chen & D. Kipping (2017).

5.2.2. Tidal Locking

Understanding whether TOI-4364b is tidally locked to its host star is crucial for accurate interpretation of the planet's atmospheric circulation patterns, atmospheric evolution (including the presence of enhanced atmospheric stripping), and thermal evolution. More specifically, when tidal forces synchronize a planet's rotation to the frequency of its orbit, the dayside of the planet receives *all* of the incident radiation, which directly impacts the aforementioned atmospheric properties (e.g., R. T. Pierrehumbert & M. Hammond 2019; J. M. Griemeier et al. 2004).

For short-period planets, tidal forces will tend to lock the planetary spin frequency to the planetary mean motion on a timescale given by

$$t_{\rm lock} \approx \frac{\omega a^6 I Q}{3 G M_\star^2 k_2 R_p^5}, \quad (3)$$

where ω is the planet's initial rotation rate, I is the moment of inertia of the planet, Q is the planet's tidal dissipation factor (a dimensionless number that describes how efficiently tidal energy is dissipated within the planet), $M_\star$ is the mass of the host star, and k_2 is the planet's Love number (which characterizes how much the planet deforms in response to tidal forces; B. Gladman et al. 1996).

Instead of solving for the tidal locking time by assuming Q, one can provide an age constraint and determine the minimum Q required for the system to not be locked. Assuming an initial rotation rate of one cycle per Earth day, a $Q \gtrsim 10^8$ is required to tidally lock the planet within 710 Myr. All the solar system planets have values much lower than this, including Uranus and Neptune ($Q \approx 10^5$; W. C. Tittemore & J. Wisdom 1990). Similarly, terrestrial planets have values much lower than this ($Q \approx$ 10–300; P. Goldreich & S. Soter 1966). As such, we can reasonably conclude that this planet is tidally locked.

5.3. Metrics for Atmospheric Characterization

Characterizing a planet's atmosphere is crucial for understanding its composition and structure. Two key metrics used to assess exoplanet atmospheres—particularly in preparation for observations with next-generation telescopes like the James Webb Space Telescope—are the transmission spectroscopy metric (TSM) and the emission spectroscopy metric (ESM). These metrics help prioritize targets for detailed follow-up studies based on the planet's ability to reveal atmospheric properties through transit and emission observations.

A fundamental parameter influencing both the TSM and ESM is the planet's equilibrium temperature, which provides a baseline for estimating atmospheric thermal structure and potential for atmospheric escape. For TOI-4364b, this temperature gives valuable insight into the energy balance of the planet and its atmospheric stability. By calculating these metrics, we can assess TOI-4364b's value as a target for transmission and emission spectroscopic follow-up. Assuming an albedo (α) of 0.3 and perfect heat redistribution, the equilibrium temperature is approximated by

$$T_{\rm eq} = T_{\rm eff}(1 - \alpha)^{\frac{1}{4}} \sqrt{\frac{R_\star}{2a}}, \quad (4)$$

where $T_{\rm eff}$ is the host star's effective temperature and $\frac{R_\star}{a}$ is the ratio of the star's radius to the semimajor axis of the planet's orbit. We calculate an equilibrium temperature of 488^{+9}_{-7} K for TOI-4364b.

The TSM evaluates the planet's suitability for transmission spectroscopy, where the atmosphere is observed as the planet passes in front of its host star, as defined in E. M. Kempton et al. (2018). For TOI-4364b, we derive a TSM of 44.2, indicating that this is a modest candidate for transmission observations when compared to the most promising TSM targets.

The ESM, which is also defined in E. M. Kempton et al. (2018), measures the planet's suitability for emission spectroscopy—the detection of thermal radiation from the planet's dayside when illuminated by its star. Using the formula from

N. B. Cowan & E. Agol (2011) for a tidally locked planet, the dayside temperature is given by

$$T_{\rm day} = \left[\frac{2}{3}(1-\alpha)\right]^{\frac{1}{4}} T_{\rm sub}, \quad (5)$$

where $T_{\rm sub}$ represents the temperature at the substellar point (the point on the planet's surface such that the host star is at the zenith) and is given by

$$T_{\rm sub} = T_{\rm eff}\left(\frac{R_\star}{a}\right)^{\frac{1}{2}}, \quad (6)$$

where $R_\star$ is the stellar radius. For TOI-4364b, we derive an ESM of 4.9, also indicating that this is a viable candidate for emission observations.

The two panels in Figure 11 illustrate the TSM and ESM values associated with TOI-4364b (calculations discussed in Section 5.3) compared to confirmed exoplanets with similar radii in the NASA Exoplanet Archive.[31] We only illustrate confirmed transiting exoplanets—planet candidates and non-transiting planets are not shown.

With reasonably strong TSM and ESM values, particularly among the population of young planets with well-constrained ages, TOI-4364b is a compelling candidate for detailed atmospheric characterization. This system has the potential to offer insights into atmospheric retention and planet formation theories in young planetary systems.

Noting its position at the upper edge of the radius valley, this planet could serve as a benchmark to test theories of atmospheric escape, investigating the relevant processes and timescales driving atmospheric loss. Valuable avenues to explore hydrodynamic escape and atmospheric mass loss include transit investigations of atomic hydrogen (Lyα; A. Vidal-Madjar et al. 2003) and metastable helium ($\lambda = 10\,830$ Å) absorption.

6. Summary

In this study, we identified and characterized TOI-4364b—a transiting mini-Neptune orbiting an M dwarf member of the Hyades cluster. This young planet is located on the upper edge of the radius valley. With a measured radius of $2.01^{+0.10}_{-0.08}\,R_\oplus$ and a relatively short orbital period, the TOI-4364b likely has an inflated atmosphere owing to its young age and high internal entropy.

The discovery of TOI-4364b adds to our growing census of planetary systems orbiting young M dwarfs. As a cluster member, this newly detected world benefits from a well-constrained stellar environment, enabling precise age estimates and meaningful comparisons with other exoplanets in similar stages of evolution. This context is crucial for understanding how planetary properties change over time under consistent stellar conditions.

As a mini-Neptune orbiting an M dwarf, there is potential to obtain a mass measurement of TOI-4364, requiring follow-up high-precision RV measurements. TOI-4364b's position near the upper edge of the radius valley offers a valuable case for studying the transition between gas-rich mini-Neptunes and rocky planets. Assuming a planetary mass of $5.3^{+1.9}_{-1.2}\,M_\oplus$ from J. Chen & D. Kipping (2017), we would expect an RV semiamplitude of $3.55^{+1.3}_{-0.93}$ m s^{-1}. Contemporary high-precision spectrographs, such as WIYN/NEID, ESPRESSO, the Habitable Zone Planet Finder, and Gemini/MaroonX, have the technological capability of detecting RV variations of this magnitude. However, a young M dwarf is expected to have high-amplitude stellar variability, potentially posing challenges for obtaining a mass measurement. A quantification of TOI-4364b's mass will help to distinguish between a gas-rich envelope and a rocky, core-dominated planet, shedding light on the processes that shape planets in this size range.

While the TSM and ESM values for this system are modest when compared to the best candidates, they are high when compared to the population of young confirmed exoplanets.

Further, the location of this M dwarf companion at the edge of the radius valley makes it a particularly compelling candidate for atmospheric characterization. TOI-4364b is well positioned for spectroscopic and outgassing observations, offering the potential to study its atmospheric composition and evolution. In conclusion, TOI-4364b represents an important addition to the study of exoplanetary systems orbiting young M dwarfs. The system characteristics offer a promising opportunity to advance our understanding of planetary atmospheres and evolutionary pathways.

Acknowledgments

We are thankful for our helpful conversations with Anne Dattilo. M.S.-F. gratefully acknowledges the generous support provided by NASA through Hubble Fellowship grant HST-HF2-51493.001-A awarded by the Space Telescope Science Institute, which is operated by the Association of Universities for Research in Astronomy, Inc., for NASA, under contract NAS 5-26555. A.W.M. was supported by grants from the NSF CAREER program (AST-2143763) and NASA's exoplanet research program (XRP 80NSSC21K0393). J.D.T. acknowledges funding support by the TESS Guest Investigator Program G06165. This paper includes data collected by the TESS mission, which are publicly available from the Mikulski Archive for Space Telescopes (MAST). Funding for the TESS mission is provided by NASA's Science Mission Directorate. All the TESS data used in this paper can be found in MAST: 10.17909/e64q-zy94. This research has made use of the Exoplanet Follow-up Observation Program (ExoFOP, NExScI 2022) website, which is operated by the California Institute of Technology, under contract with the National Aeronautics and Space Administration under the Exoplanet Exploration Program. Some of the observations in the paper made use of the High-Resolution Imaging instruments 'Alopeke and Zorro. 'Alopeke and Zorro were funded by the NASA Exoplanet Exploration Program and built at the NASA Ames Research Center by Steve B. Howell, Nic Scott, Elliott P. Horch, and Emmett Quigley. 'Alopeke was mounted on the Gemini North telescope, and telescope Zorro was mounted on the Gemini South telescope, both a part of the international Gemini Observatory, a program of NSF NOIRLab, which is managed by the Association of Universities for Research in Astronomy (AURA) under a cooperative agreement with the US National Science Foundation on behalf of the Gemini Observatory partnership: the US National Science Foundation (United States), National Research Council (Canada), Agencia Nacional de Investigación y Desarrollo (Chile), Ministerio de Ciencia, Tecnologìa e Innovación (Argentina), Ministério da Ciência, Tecnologia, Inovações e Comunicações (Brazil), and

[31] https://exoplanetarchive.ipac.caltech.edu/

Korea Astronomy and Space Science Institute (Republic of Korea). This work has made use of data from the European Space Agency (ESA) mission Gaia,[32] processed by the Gaia Data Processing and Analysis Consortium (DPAC).[33] This research has made use of the VizieR catalog access tool, CDS, Strasbourg, France. The original description of the VizieR service was published in A&AS 143, 23. We acknowledge the use of public TOI Release data from pipelines at the TESS Science Office and the TESS Science Processing Operations Center. Resources supporting this work were provided by the NASA High-End Computing (HEC) Program through the NASA Advanced Supercomputing (NAS) Division at Ames Research Center for the production of the SPOC data products. This work made use of `tpfplotter` by J. Lillo-Box (publicly available in www.github.com/jlillo/tpfplotter), which also made use of the Python packages `astropy`, `lightkurve`, `matplotlib`, and `numpy`.

This publication makes use of data products from the Two Micron All Sky Survey, which is a joint project of the University of Massachusetts and the Infrared Processing and Analysis Center/California Institute of Technology, funded by the National Aeronautics and Space Administration and the National Science Foundation. This work makes use of observations from the LCOGT network. Part of the LCOGT telescope time was granted by NOIRLab through the Mid-Scale Innovations Program (MSIP). MSIP is funded by NSF. Based in part on observations obtained at the Southern Astrophysical Research (SOAR) telescope, which is a joint project of the Ministério da Ciência, Tecnologia e Inovações (MCTI/LNA) do Brasil, the US National Science Foundation's NOIRLab, the University of North Carolina at Chapel Hill (UNC), and Michigan State University (MSU). Funding for the TESS mission is provided by NASA's Science Mission Directorate. The postdoctoral fellowship of K.B. is funded by F.R.S.-FNRS grant T.0109.20 and by the Francqui Foundation. The Dunlap Institute is funded through an endowment established by the David Dunlap family and the University of Toronto. K.A.C. and S.N.Q. acknowledge support from the TESS mission via subaward s3449 from MIT.

Facilities: TESS, Gaia DR3 (Gaia Collaboration et al. 2021); Mikulski Archive for Space Telescopes (A. Marston et al. 2018); Wide-field Infrared Survey Explorer (WISE); LCOGT 1 m (Sinistro); LCOGT 1 m (NRES); Gemini: Gillett, South; Very Large Telescope; Southern Astrophysical Research (SOAR) Telescope.

Software: `AstroImageJ` (K. A. Collins et al. 2017), `astroquery` (A. Ginsburg et al. 2019), BANZAI (C. McCully et al. 2018), `batman` (L. Kreidberg 2015), `dustmaps` (G. Green 2018), `edmcmc` (A. Vanderburg 2021), `EXOFASTv2` (J. Eastman et al. 2013), galpy (J. Bovy 2015), `Lightkurve` (Lightkurve Collaboration et al. 2018), `matplotlib` (J. D. Hunter 2007), `PAdova and TRieste Stellar Evolution Code` (A. Bressan et al. 2012), `PyAstronomy` (S. Czesla et al. 2019), `starrotate` (R. Angus & A. Garcia Soto 2023), `TRICERATOPS` (S. Giacalone et al. 2021), `TESSCUT` (C. E. Brasseur et al. 2019), `Vplanet` (R. Barnes et al. 2020).

[32] https://www.cosmos.esa.int/gaia
[33] https://www.cosmos.esa.int/web/gaia/dpac/consortium

ORCID iDs

Adam Distler https://orcid.org/0009-0006-4294-6760
Melinda Soares-Furtado https://orcid.org/0000-0001-7493-7419
Andrew Vanderburg https://orcid.org/0000-0001-7246-5438
Jack Schulte https://orcid.org/0000-0002-7382-0160
Juliette Becker https://orcid.org/0000-0002-7733-4522
Andrew W. Mann https://orcid.org/0000-0003-3654-1602
Steve B. Howell https://orcid.org/0000-0002-2532-2853
Adam L. Kraus https://orcid.org/0000-0001-9811-568X
Ronan Kerr https://orcid.org/0000-0002-6549-9792
Khalid Barkaoui https://orcid.org/0000-0003-1464-9276
César Briceño https://orcid.org/0000-0001-7124-4094
Karen A. Collins https://orcid.org/0000-0001-6588-9574
Dennis Conti https://orcid.org/0000-0003-2239-0567
Jon M. Jenkins https://orcid.org/0000-0002-4715-9460
Mary Anne Limbach https://orcid.org/0000-0002-9521-9798
Samuel N. Quinn https://orcid.org/0000-0002-8964-8377
Richard P. Schwarz https://orcid.org/0000-0001-8227-1020
Sara Seager https://orcid.org/0000-0002-6892-6948
Jake D. Turner https://orcid.org/0000-0001-7836-1787
Joseph D. Twicken https://orcid.org/0000-0002-6778-7552
Joshua N. Winn https://orcid.org/0000-0002-4265-047X
Carl Ziegler https://orcid.org/0000-0002-0619-7639

References

Adams, F. C., & Laughlin, G. 2006, ApJ, 649, 1004
Aller, A., Lillo-Box, J., Jones, D., Miranda, L. F., & Forteza, S. B. 2020, A&A, 635, A128
Angus, R., & Garcia Soto, A. 2023, agarciasoto18/starrotate: Alternate Starrotate for Paper, v1.1, Zenodo, doi:10.5281/zenodo.7697238
Baraffe, I., Homeier, D., Allard, F., & Chabrier, G. 2015, A&A, 577, A42
Barnes, R., Luger, R., Deitrick, R., et al. 2020, PASP, 132, 024502
Bovy, J. 2015, ApJS, 216, 29
Brandeker, A., & Cataldi, G. 2019, A&A, 621, A86
Brandner, W., Calissendorff, P., & Kopytova, T. 2023, MNRAS, 518, 662
Brasseur, C. E., Phillip, C., Fleming, S. W., Mullally, S. E., & White, R. L., 2019 Astrocut: Tools for creating cutouts of TESS images, Astrophysics Source Code Library, ascl:1905.007
Bressan, A., Marigo, P., Girardi, L., et al. 2012, MNRAS, 427, 127
Brown, T. M., Baliber, N., Bianco, F. B., et al. 2013, PASP, 125, 1031
Buchhave, L. A., Bakos, G. A., Hartman, J. D., et al. 2010, ApJ, 720, 1118
Burn, R., Mordasini, C., Mishra, L., et al. 2024, NatAs, 8, 463
Cautun, M., Benìtez-Llambay, A., Deason, A. J., et al. 2020, MNRAS, 494, 4291
Chambers, J. E., & Wetherill, G. W. 1998, Icar, 136, 304
Chen, J., & Kipping, D. 2017, ApJ, 834, 17
Ciardi, D. R., Beichman, C. A., Horch, E. P., & Howell, S. B. 2015, ApJ, 805, 16
Ciardi, D. R., Crossfield, I. J. M., Feinstein, A. D., et al. 2018, AJ, 155, 10
Collins, K. A., Kielkopf, J. F., Stassun, K. G., & Hessman, F. V. 2017, AJ, 153, 77
Cowan, N. B., & Agol, E. 2011, ApJ, 726, 82
Curtis, J. L., Ageros, M. A., Douglas, S. T., & Meibom, S. 2019, ApJ, 879, 49
Cutri, R. M., Wright, E. L., Conrow, T., et al. 2012, yCat, II/311
Cutri, R. M., Skrutskie, M. F., van Dyk, S., et al. 2003, yCat, 11/246
Czesla, S., Schröter, S., Schneider, C. P., et al., 2019 PyA: Python astronomy-related packages, Astrophysics Source Code Library, ascl:1906.010
Dehnen, W., & Binney, J. 1998, MNRAS, 294, 429
Dorn, C., Noack, L., & Rozel, A. B. 2018, A&A, 614, A18
Douglas, S. T., Ageros, M. A., Covey, K. R., et al. 2014, ApJ, 795, 161
Douglas, S. T., Agüeros, M. A., Covey, K. R., & Kraus, A. 2017, ApJ, 842, 83
Eastman, J., Gaudi, B. S., & Agol, E. 2013, PASP, 125, 83
Eastman, J. D., Rodriguez, J. E., Agol, E., et al. 2019, arXiv:1907.09480
Erkaev, N. V., Kulikov, Y. N., Lammer, H., et al. 2007, A&A, 472, 329
Fűrész, G. 2008, PhD thesis, Univ. of Szeged

Freund, S., Robrade, J., Schneider, P. C., & Schmitt, J. H. 2020, A&A, 640, A66
Fulton, B. J., Petigura, E. A., Howard, A. W., et al. 2017, AJ, 154, 109
Furlan, E., & Howell, S. B. 2017, AJ, 154, 66
Furlan, E., & Howell, S. B. 2020, AJ, 898, 47
Gaia Collaboration, Brown, A. G. A., Vallenari, A., et al. 2021, A&A, 649, A1
Gaia Collaboration, Prusti, T., de Bruijne, J., et al. 2016, A&A, 595, A1
Gelman, A., & Rubin, D. B. 1992, StaSc, 7, 457
Giacalone, S., Dressing, C. D., Jensen, E. L. N., et al. 2021, AJ, 161, 24
Ginsburg, A., Sipőcz, B.M., Brasseur, C.E., et al. 2019, AJ, 157, 98
Ginzburg, S., Schlichting, H. E., & Sari, R. 2018, MNRAS, 476, 759
Gladman, B., Quinn, D. D., Nicholson, P., & Rand, R. 1996, Icar, 122, 166
Goldreich, P., & Soter, S. 1966, Icar, 5, 375
Gossage, S., Conroy, C., Dotter, A., et al. 2018, ApJ, 863, 67
Gossage, S., Kalogera, V., & Sun, M. 2023, ApJ, 950, 27
Green, G. 2018, JOSS, 3, 695
Green, G. M., Schlafly, E., Zucker, C., Speagle, J. S., & Finkbeiner, D. 2019, ApJ, 887, 93
Green, G. M., Schlafly, E. F., Finkbeiner, D. P., et al. 2015, ApJ, 810, 25
Grießmeier, J. M., Stadelmann, A., Penz, T., et al. 2004, A&A, 425, 753
Hippke, M., & Heller, R. 2019, A&A, 623, A39
Howell, S. B., Everett, M. E., Sherry, W., Horch, E., & Ciardi, D. R. 2011, AJ, 142, 19
Hunter, J. D. 2007, CSE, 9, 90
Irrgang, A., Wilcox, B., Tucker, E., & Schiefelbein, L. 2013, A&A, 549, A137
Jenkins, J. M. 2002, ApJ, 575, 493
Jenkins, J. M., Chandrasekaran, H., McCauliff, S.D., et al. 2010, Proc. SPIE, 7740, 77400D
Jenkins, J. M., Tenenbaum, P., Seader, S., et al. 2020, in Kepler Data Processing Handbook, ed. J. M. Jenkins (Washington, DC: NASA), 9
Jenkins, J. M., Twicken, J. D., McCauliff, S., et al. 2016, Proc. SPIE, 9913, 99133E
Johnson, D. R. H., & Soderblom, D. R. 1987, AJ, 93, 864
Kempton, E. M., Bean, J. L., Louie, D. R., et al. 2018, PASP, 130, 114401
Kipping, D. 2023, MNRAS, 523, 1182
Kite, E. S., Manga, M., & Gaidos, E. 2009, ApJ, 700, 1732
Kovács, G., Zucker, S., & Mazeh, T. 2002, A&A, 391, 369
Kreidberg, L. 2015, PASP, 127, 1161
Li, J., Tenenbaum, P., Twicken, J. D., et al. 2019, PASP, 131, 024506
Lightkurve Collaboration, Cardoso, J.V.D.M., Hedges, C., et al., 2018 Lightkurve: Kepler and TESS time series analysis in Python, Astrophysics Source Code Library, ascl:1812.013
Lodieu, N., Smart, R. L., Prez-Garrido, A., & Silvotti, R. 2019, A&A, 623, A35
Lomb, N. R. 1976, Ap&SS, 39, 447
Long, L., Bi, S., Zhang, J., et al. 2023, ApJS, 268, 30
Lopez, E. D., & Fortney, J. J. 2014, ApJ, 792, 1
Lopez, E. D., Fortney, J. J., & Miller, N. 2012, ApJ, 761, 59
Luger, R., & Barnes, R. 2015, AsBio, 15, 119
Mann, A. W., Newton, E. R., Rizzuto, A. C., et al. 2016, AJ, 152, 61
Mann, A. W., Vanderburg, A., Rizzuto, A. C., et al. 2018, AJ, 155, 4
Marston, A., Hargis, J., Levay, K., et al. 2018, Proc. SPIE, 10704, 1070413
Mayo, A. W., Dressing, C. D., Vanderburg, A., et al. 2023, AJ, 165, 235
McCully, C., Volgenau, N.H., Harbeck, D.R., et al. 2018, Proc. SPIE, 10707, 107070K
McMillan, P. J. 2017, MNRAS, 465, 76
Mestel, L. 1968, MNRAS, 140, 177
Mignon, L., Meunier, N., Delfosse, X., et al. 2023, A&A, 675, A168
Morbidelli, A., Lunine, J. I., O'Brien, D. P., Raymond, S. N., & Walsh, K. J. 2012, AREPS, 40, 251
Morris, R. L., Twicken, J. D., Smith, J. C., et al. 2020, in Kepler Data Processing Handbook, ed. J. M. Jenkins (Washington, DC: NASA)
Newton, E. R., Mann, A. W., Tofflemire, B. M., et al. 2019, ApJL, 880, L17
NExScI 2022, Exoplanet Follow-up Observing Program Web Service, IPAC, doi:10.26134/EXOFOP5
Oh, S., & Evans, N. W. 2020, MNRAS, 498, 1920
Owen, J. E., & Wu, Y. 2017, ApJ, 847, 29
Pepe, F., Cristiani, S., Rebolo, R., et al. 2021, A&A, 645, A96
Pierrehumbert, R. T., & Hammond, M. 2019, AnRFM, 51, 275
Quinn, S. N., White, R. J., Latham, D. W., et al. 2014, ApJ, 787, 27
Rebull, L. M., Stauffer, J. R., Bouvier, J., et al. 2016, AJ, 152, 113
Ricker, G. R., Winn, J. N., Vanderspek, R., et al. 2015, JATIS, 1, 014003
Rogers, L. A. 2015, ApJ, 801, 41
Röser, S., Schilbach, E., & Goldman, B. 2019, A&A, 621, L2
Sato, B., Izumiura, H., Toyota, E., et al. 2007, ApJ, 661, 527
Scargle, J. D. 1982, ApJ, 263, 835
Scott, N. J., Howell, S. B., Gnilka, C. L., et al. 2021, FrASS, 8, 138
Skumanich, A. 1972, ApJ, 171, 565
Smith, J. C., Stumpe, M. C., Van Cleve, J. E., et al. 2012, PASP, 124, 1000
Stefansson, G., Mahadevan, S., Maney, M., et al. 2020, AJ, 160, 192
Stellingwerf, R. F. 1978, ApJ, 224, 953
Stumpe, M. C., Smith, J. C., Catanzarite, J. H., et al. 2014, PASP, 126, 100
Stumpe, M. C., Smith, J. C., Van Cleve, J. E., et al. 2012, PASP, 124, 985
Szentgyorgyi, A. H., & Fursz, G. 2007, RMxAA, 28, 129
Tabernero, H. M., Montes, D., & Hernndez, J. I. G. 2012, A&A, 547, A13
Tarricq, Y., Soubiran, C., Casamiquela, L., et al. 2021, A&A, 647, A19
Teng, H. Y., Sato, B., Kuzuhara, M., et al. 2023, PASJ, 75, 1030
Tittemore, W. C., & Wisdom, J. 1990, Icar, 85, 394
Tokovinin, A. 2018, PASP, 130, 035002
Twicken, J. D., Catanzarite, J. H., Clarke, B. D., et al. 2018, PASP, 130, 064502
Twicken, J.D., & Wisdom, J. 2010, Proc. SPIE, 7740, 774023
Vanderburg, A. 2021, avanderburg/edmcmc: v1.0.0, Zenodo, doi:10.5281/zenodo.5599854
Vanderburg, A., Huang, C. X., Rodriguez, J. E., et al. 2019, ApJL, 881, L19
Vanderburg, A., Mann, A. W., Rizzuto, A., et al. 2018, AJ, 156, 46
Vidal-Madjar, A., Lecavelier des Etangs, A., Désert, J. M., et al. 2003, Natur, 422, 143
Watson, A. J., Donahue, T. M., & Walker, J. C. G. 1981, Icar, 48, 150
Winters, J. G., Henry, T. J., Jao, W.-C., et al. 2019, AJ, 157, 216
Wright, E. L., Eisenhardt, P. R. M., Mainzer, A. K., et al. 2010, AJ, 140, 1868
Zacharias, N., Finch, C. T., Girard, T. M., et al. 2013, AJ, 145, 44
Ziegler, C., Tokovinin, A., Briceño, C., et al. 2020, AJ, 159, 19